

# Supplementary Information: Emergent collective chemotaxis without single-cell gradient sensing

Brian A. Camley

Juliane Zimmermann

Herbert Levine

Wouter-Jan Rappel

## 1 Cluster chemotaxis when chemoattractant regulates cell persistence $\tau$

Within the main paper, we have assumed that the chemoattractant concentration  $S(\mathbf{r})$  regulates the susceptibility of a cell to contact inhibition of locomotion  $\beta^i$ , with  $\beta^i = \bar{\beta}S(\mathbf{r}^i)$ . This models the stabilization of protrusions induced by contact interactions. This is consistent with the results of Theveneau et al. [1], who find that protrusion stabilization is stronger in clusters than in single cells. However, very similar results can be found if we assume that  $\beta$  is constant and the signal regulates the time required for the cell's polarity to relax, i.e.  $\tau^i = \bar{\tau}S(\mathbf{r})$ . In this case, the mean polarity of a cell is  $\langle \mathbf{p}^i \rangle = \beta\tau^i \sum_{j \sim i} \hat{\mathbf{r}}^{ij}$  and we find

$$\langle \mathbf{V} \rangle \approx \beta\bar{\tau}\mathcal{M} \cdot \nabla S \quad (\tau \text{ regulation}) \quad (\text{S1})$$

where the mobility matrix  $\mathcal{M}$  is the same as in the main paper,  $\mathcal{M}_{\mu\nu} = \frac{1}{N} \sum_i r_\nu^i q_\mu^i$ . However, because  $\tau$  varies over space, the fluctuations will also vary:  $\langle (V_\mu - \langle V_\mu \rangle)^2 \rangle = \sigma^2 N^{-2} \sum_i \tau^i = \sigma^2 N^{-1} \bar{\tau} \bar{S}$ , where  $\bar{S} = N^{-1} \sum_i S(\mathbf{r}^i)$  is the mean signal across the cluster. For this reason, the chemotactic index in the  $\tau$ -regulation model will depend on  $\nabla S / \bar{S}^{1/2}$ , and will not be constant over a linear gradient.

In addition, a single cell with a persistence time  $\tau$  that depends on the chemoattractant level will undergo biased motion. This is shown in Fig. S1 below. This drift can be made smaller than the CIL-driven cluster drift, as it is independent of  $\beta$ , while the cluster drift is proportional to  $\beta$ .

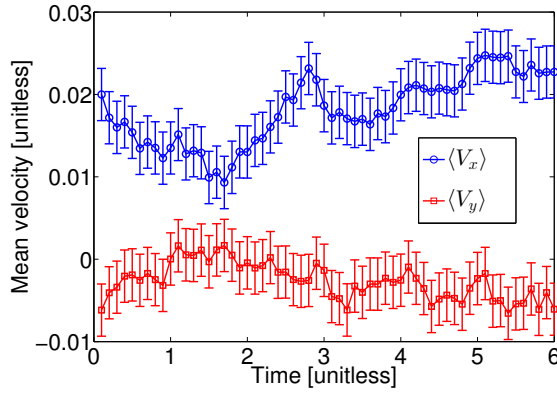


Figure S1: **Single cells in a spatially-varying  $\tau$  develop a mean drift.** The mean  $x$  and  $y$  velocities for a cell with spatially varying  $\tau$  are shown:  $\tau = \bar{\tau}(S_0 + |\nabla S|x)$ , with  $\bar{\tau} = 1$ ,  $S_0 = 1$ ,  $|\nabla S| = 0.025$ . Result is average over  $n = 10^5$  iterations, each started at the origin; error bars indicate  $\langle [V_\mu(t) - \langle V_\mu(t) \rangle]^2 \rangle^{1/2} / \sqrt{n}$ .

## 2 Derivation of the mobility matrices for $Q$ -layer oligomers

We can compute the mobility matrix of the  $Q$ -layer oligomers for arbitrary  $Q$ . Our mobility matrix is given by

$$\mathcal{M}_{\mu\nu} = \frac{1}{N} \sum_i q_\mu^i r_\nu^i \quad (\text{S2})$$

with  $\mathbf{q}^i = \sum_{j \sim i} \hat{\mathbf{r}}^{ij}$ . To simplify the calculation, we can make a few assumptions. First, we note that  $\mathcal{M}_{xx} = \mathcal{M}_{yy}$ , but  $\mathcal{M}_{xy} = \mathcal{M}_{yx} = 0$  for the  $Q$ -layer oligomer. We only need to calculate  $\bar{\mathcal{M}} = \frac{1}{2}(\mathcal{M}_{xx} + \mathcal{M}_{yy})$ . The only cells  $i$  in the sum of Eq. S2 that are nonzero are those around the boundary.  $\bar{\mathcal{M}}$  does not depend on orientation, so we can compute the sum  $\sum_i \mathbf{r}^i \mathbf{q}^i$  for one face of the oligomer (Fig. S2), then multiply by six. However, this double-counts the corner cells, so we must

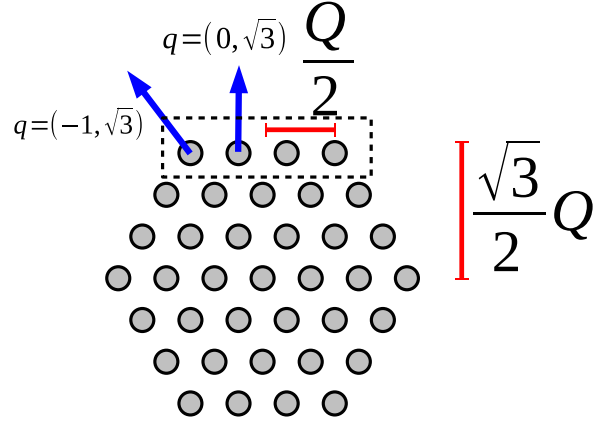


Figure S2: **Geometry of  $Q$ -layer oligomer, illustrated for  $Q = 3$ .** The top face is highlighted by a dashed line.

weight them by  $1/2$ . We then find  $\overline{\mathcal{M}} = [\frac{9}{2}Q^2 + \frac{3}{2}Q] / N(Q)$ , where  $N(Q) = 1 + 3Q + 3Q^2$  is the number of cells in the cluster.

We present the mobility matrices for both  $Q$ -layer oligomers and other cluster shapes in Table S1.






Shape	$\mathcal{M}$	Angularly averaged $\overline{\mathcal{M}}$
Dimer 	$\begin{pmatrix} 1/2 & 0 \\ 0 & 0 \end{pmatrix}$	$1/4$
Trimer 	$\begin{pmatrix} 1/2 & 0 \\ 0 & 1/2 \end{pmatrix}$	$1/2$
Tetramer 	$\begin{pmatrix} 1/2 & 0 \\ 0 & 3/4 \end{pmatrix}$	$5/8$
Heptamer 	$\begin{pmatrix} 6/7 & 0 \\ 0 & 6/7 \end{pmatrix}$	$6/7$
$Q$ -layer oligomer 	$\begin{pmatrix} f(Q) & 0 \\ 0 & f(Q) \end{pmatrix}$	$f(Q) \equiv \frac{9Q^2 + 3Q}{2 + 6Q + 6Q^2}$

Table S1: **Mobility matrices  $\mathcal{M}$  for several cell configurations.** For each of the configurations shown, nearest-neighbor cells have unit separation. A  $Q$ -layer oligomer has  $N(Q) = 1 + 3Q + 3Q^2$  cells.  $\mathcal{M}$  is given for the orientation shown in the left column; other orientations may be found by transforming the mobility tensor;  $\overline{\mathcal{M}} = \frac{1}{2}(\mathcal{M}_{xx} + \mathcal{M}_{yy})$  (see Section 3 below).

### 3 Rotational transformation and averaging of the mobility matrix

We can compute the mobility matrix of a rotated cluster of arbitrary shape from Eq. S2. If we rotate our cluster, which we assume is centered at the origin, by an angle  $\theta$ ,  $(\mathbf{r}^i)^j = \mathcal{R}(\theta)\mathbf{r}^i$ , we find that

$$\mathcal{M}'_{\mu\nu} = \mathcal{R}_{\mu\alpha}(\theta)\mathcal{M}_{\alpha\beta}\mathcal{R}_{\nu\beta}(\theta) \quad (\text{S3})$$

where we have assumed the Einstein summation convention and  $\mathcal{R}(\theta)$  is the rotation matrix  $\begin{pmatrix} \cos \theta & -\sin \theta \\ \sin \theta & \cos \theta \end{pmatrix}$ . In matrix terms,  $\mathcal{M}' = \mathcal{R}(\theta) \cdot \mathcal{M} \cdot [\mathcal{R}(\theta)]^T$ . If we average over  $\theta$ , we find

$$\frac{1}{2\pi} \int_0^{2\pi} d\theta \mathcal{M}'(\theta) = \frac{1}{2} \begin{pmatrix} \mathcal{M}_{xx} + \mathcal{M}_{yy} & \mathcal{M}_{xy} - \mathcal{M}_{yx} \\ \mathcal{M}_{yx} - \mathcal{M}_{xy} & \mathcal{M}_{xx} + \mathcal{M}_{yy} \end{pmatrix} \quad (\text{S4})$$

We can show from the definition Eq. S2 that  $\mathcal{M}_{\mu\nu} = \mathcal{M}_{\nu\mu}$ , so the off-diagonal entries of the averaged matrix are zero, and therefore  $\frac{1}{2\pi} \int_0^{2\pi} d\theta \mathcal{M}'_{\mu\nu}(\theta) = \frac{1}{2}(\mathcal{M}_{xx} + \mathcal{M}_{yy})\delta_{\mu\nu}$ . In other words, when averaged over orientation, a cell cluster's mobility matrix is just the constant  $\overline{\mathcal{M}}$  times the identity.

## 4 Computing the chemotactic index

We showed in the main paper that within our model, assuming that the cluster rearrangement is slow with respect to the polarity dynamics and thus each cell's polarity is given by a biased Ornstein-Uhlenbeck process, the velocity of a rigid cell cluster is

$$\mathbf{V} = \langle \mathbf{V} \rangle + \Delta \quad (\text{S5})$$

where  $\Delta$  is a Gaussian random variable with zero mean and variance  $\langle \Delta_\mu \Delta_\nu \rangle = \Gamma^2 \delta_{\mu\nu}$ . We want to compute the chemotactic index, CI; assuming the gradient is increasing in the  $x$  direction, this is

$$\text{CI} = \frac{\langle V_x \rangle}{\langle |\mathbf{V}| \rangle} \quad (\text{S6})$$

where the average is both over time and over many trajectories. We note that this is a useful definition for us because, in our model, neither  $\langle \mathbf{V} \rangle$  nor  $\Delta$  depend on the absolute value of the chemoattractant  $S$ . More care must be taken in other cases. To compute CI, we need to compute  $\langle |\mathbf{V}| \rangle$ .  $|\mathbf{V}|$  is, in our case, given by a Rice distribution, and this moment can be calculated.

$$\langle |\mathbf{V}| \rangle = \langle \sqrt{(\langle V_x \rangle + \Delta_x)^2 + (\langle V_y \rangle + \Delta_y)^2} \rangle \quad (\text{S7})$$

$$= \frac{1}{2\pi\Gamma^2} \int d\Delta_x d\Delta_y \sqrt{(\langle V_x \rangle + \Delta_x)^2 + (\langle V_y \rangle + \Delta_y)^2} \exp\left[-\frac{(\Delta_x^2 + \Delta_y^2)}{2\Gamma^2}\right] \quad (\text{S8})$$

$$= \frac{1}{2\pi\Gamma^2} \int dV_x dV_y V \exp\left[-\frac{1}{2\Gamma^2} \{(V_x - \langle V_x \rangle)^2 + (V_y - \langle V_y \rangle)^2\}\right] \quad (\text{S9})$$

where  $V = \sqrt{V_x^2 + V_y^2}$ . We now switch to polar coordinates,  $V_x = V \cos \phi$ ,  $V_y = V \sin \phi$ , and correspondingly write  $\langle V_x \rangle = \nu \cos \theta$  and  $\langle V_y \rangle = \nu \sin \theta$ , where  $\nu^2 = \langle V_x \rangle^2 + \langle V_y \rangle^2$ . Thus,

$$\langle |\mathbf{V}| \rangle = \frac{1}{2\pi\Gamma^2} \int_0^{2\pi} d\phi \int_0^\infty dV V^2 \exp\left[-\frac{1}{2\Gamma^2} \{V^2 + \nu^2 - 2V\nu \cos(\theta - \phi)\}\right] \quad (\text{S10})$$

$$= \frac{1}{\Gamma^2} \int_0^\infty dV V^2 \exp\left[-\frac{1}{2\Gamma^2} (V^2 + \nu^2)\right] I_0(V\nu/\Gamma^2) \quad (\text{S11})$$

where  $I_0(x)$  is the modified Bessel function of the first kind. This integral may be evaluated, resulting in

$$\langle |\mathbf{V}| \rangle = \Gamma \sqrt{\pi/2} L_{1/2}(-\nu^2/2\Gamma^2) \quad (\text{S12})$$

where the generalized Laguerre polynomial  $L_{1/2}$  is given by

$$L_{1/2}(x) = e^{x/2} [(1-x)I_0(-x/2) - xI_1(-x/2)]. \quad (\text{S13})$$

Within our average over trajectories, we are averaging over the orientation of the cluster; thus we expect  $\langle V_y \rangle = 0$  for a chemoattractant gradient in the  $x$  direction, and  $\nu = \langle V_x \rangle = \bar{\beta}\tau\overline{\mathcal{M}}\partial_x S$ .  $\Gamma^2 = \langle (V_x - \langle V_x \rangle)^2 \rangle = \langle (V_y - \langle V_y \rangle)^2 \rangle = \sigma^2\tau/N$ . This leads to the result stated in the main paper,

$$\begin{aligned} \text{CI} &= \sqrt{2/\pi} c / L_{1/2}(-c^2/2) \\ c &= \frac{\langle V_x \rangle}{\sqrt{\langle (V_x - \langle V_x \rangle)^2 \rangle}} = \frac{\bar{\beta}\tau\overline{\mathcal{M}}\partial_x S}{\sigma\sqrt{\tau/N}} \end{aligned} \quad (\text{S14})$$

where in our notation, we could also write  $c = \nu/\Gamma$ . We plot the result of Eq. S14 in Fig. S3 below; we see that  $\text{CI} \rightarrow 1$  as  $c \gg 1$  (corresponding to cluster velocities much larger than the noise in cluster velocity) and  $\text{CI} \rightarrow 0$  if  $|c| \ll 1$  (cluster velocity much smaller than the noise). We also note that chemotaxis could oppose the direction of the gradient (chemorepulsion) – in this case,  $\text{CI}(-c) = -\text{CI}(c)$ .

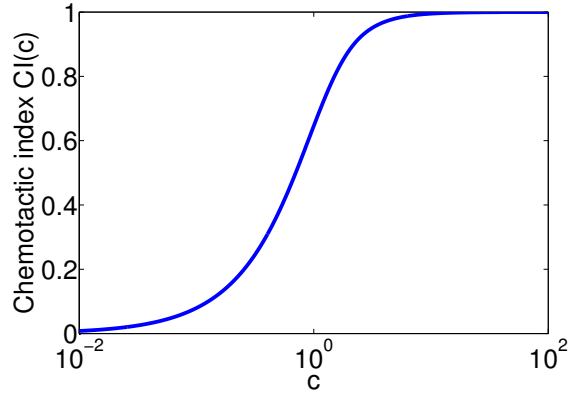


Figure S3: **Chemotactic index CI as a function of the parameter  $c$ .**

## 5 Velocity and CI of irregular clusters

In the main paper, we presented results on the velocity and chemotactic index of  $Q$ -layer oligomers. Here, we show the velocity and chemotactic index of imperfect clusters. We begin with a  $Q$ -layer oligomer, and then remove  $n$  cells at random from the outer layer; this process is repeated 200 times for each  $n$  from 1 to  $6Q$  (the number of cells in the outer layer). An example is presented in Fig. S4, with  $Q = 5$  and  $n = 5$  cells removed. The mobility matrix is computed for each cluster, and used to compute  $\langle V_x \rangle$  and CI (Fig. S4). We see that though different configurations can lead to different mean velocities for the same number of cells, the general trend is captured by the results for intact oligomers (dashed line and square symbols in Fig. S4).

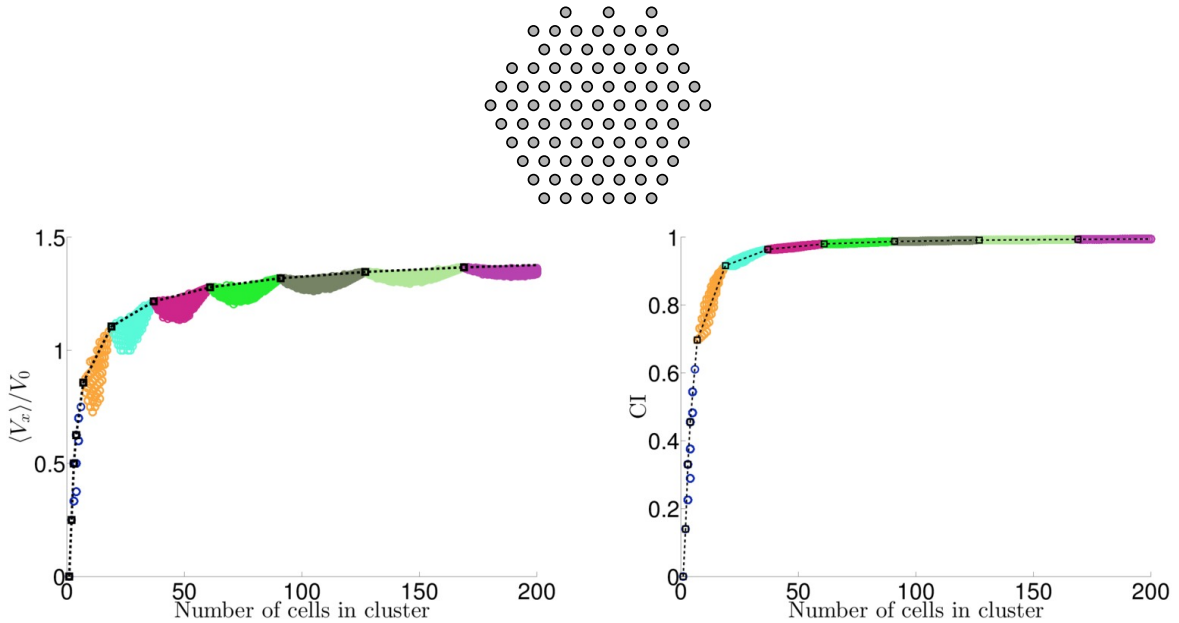


Figure S4: **Cluster shape effects, in addition to cell number, can affect velocity and CI.** Top: illustration of  $Q$ -layer oligomer with a few cells removed from the external layer. Bottom: Velocity and chemotactic index for clusters of different shapes. Different colors indicate the size of the base cluster from which cells are removed. Black squares connected by dashed lines show the results for intact oligomers. For the CI plot, we apply our usual parameters and  $|\nabla S| = 0.025$ . All results in this figure are theoretical results for rigid clusters only, not full simulations.

## 6 Transient rotation of clusters

Though we have primarily focused on the translational motion of the cluster, rotational motion can also occur in our model, both through rotational diffusion and biased motion. We note that transient rotational events are observed in [2]. Under assumptions similar to our main results, clusters have mean angular velocity  $\sim \mathbf{A} \cdot \nabla S$ , where  $\mathbf{A}$  depends on cluster geometry. This is again similar to an oddly-shaped particle sedimenting in a low Reynolds number flow [3]. However, the symmetric

clusters in Table S1 have  $\mathbf{A} = \mathbf{0}$  and do not rotate. If  $\mathbf{A} \neq \mathbf{0}$ , clusters rotate to a fixed angle to the gradient direction; there is no persistent rotation in a linear gradient (rotational motion may also be suppressed if  $\bar{\beta}$  is large). However, in nonlinear gradients, persistent rotation of asymmetric clusters may be induced.

We can analyze potential biases by determining the net ‘torque’  $L_z = \sum_i [\delta \mathbf{r}^i \times \mathbf{p}^i]_z$  applied to the cluster by the cells. This torque is, on average,

$$\langle L_z \rangle = \sum_i \bar{\beta} \tau S(\mathbf{r}^i) [\delta \mathbf{r}^i \times \mathbf{q}^i]_z \quad (\text{S15})$$

where  $\mathbf{q}^i = \sum_{j \sim i} \hat{\mathbf{r}}^{ij}$  and  $\delta \mathbf{r}^i = \mathbf{r}^i - \mathbf{r}_{\text{cm}}$  is the displacement from the cluster center of mass.

What torque is required to cause the cluster to move at a fixed angular velocity? For a cluster moving in a rigid rotation with angular velocity  $\Omega$ , the cell velocities are  $\mathbf{v}^i = \Omega (-\delta r_y^i, \delta r_x^i)$ . To achieve this, each cell must have a polarity of  $\mathbf{p}^i = \Omega (-\delta r_y^i, \delta r_x^i)$ , leading to  $L_z = \Omega \sum_i |\delta \mathbf{r}^i|^2$ . The angular velocity is thus related to  $L_z$  by  $\Omega = L_z / \sum_i |\delta \mathbf{r}^i|^2$ . We thus find, for linear gradients,  $S = S_0 + \mathbf{r} \cdot \nabla S$ ,

$$\langle \Omega \rangle = \bar{\beta} \tau \mathbf{A} \cdot \nabla S \quad (\text{S16})$$

where the vector  $\mathbf{A}$  only depends on the cluster geometry,

$$\mathbf{A} = \frac{\sum_i \delta \mathbf{r}^i [\delta \mathbf{r}^i \times \mathbf{q}^i]_z}{\sum_i |\delta \mathbf{r}^i|^2} \quad (\text{S17})$$

where  $\mathbf{q}^i$  is defined as above. (Note that  $\sum_i \delta \mathbf{r}^i \times \mathbf{q}^i = \sum_i \mathbf{r}^i \times \mathbf{q}^i = -\sum_{i,j \sim i} \frac{\mathbf{r}^i \times \mathbf{r}^j}{|\mathbf{r}^i - \mathbf{r}^j|} = 0$ , allowing us to drop a center of mass term.) For all of the shapes listed in Table S1,  $\mathbf{A} = \mathbf{0}$ . Cell clusters must lack an inversion symmetry to be rotated by the gradient.

However, even if  $\mathbf{A} \neq \mathbf{0}$ , clusters will not persistently rotate. We can see that if we rotate the cell cluster around its center of mass,  $\mathbf{A}$  must also rotate as a vector. If the gradient is along the  $x$  direction, this lets us write  $\langle \Omega \rangle = \langle \dot{\theta} \rangle = \bar{\beta} \tau [A_x(0) \cos \theta - A_y(0) \sin \theta]$ , where  $\mathbf{A}(0)$  is Eq. S17 calculated for a reference geometry. We see that if  $\mathbf{A} \neq \mathbf{0}$ , the cluster will rotate to a stable angle  $\theta^*$  given by  $\tan \theta^* = A_x(0)/A_y(0)$ . In a linear gradient, there is no persistent rotation, though in nonlinear gradients, persistent rotation of asymmetric clusters may be induced.

We note that Eq. S16 is not as quantitatively accurate as the corresponding result for translational motion, at least for the parameter set in the main paper; this occurs because a small deviation from the equilibrium polarity  $\langle \mathbf{p}^i \rangle$  can create a relatively large change in torque, which often resists rotation. For instance, if the cluster is rotated by a small angle  $\delta$  without a corresponding change in  $\langle \mathbf{p}^i \rangle$ , there will be a restoring torque proportional to  $\bar{\beta} \tau \delta$ . Thus, Eq. S16 will be more accurate for systems where the relaxation time  $\tau$  is smaller compared to the rotational timescale of the cluster. For similar reasons, for our rigid cluster parameter set, rotational diffusion can be quite slow (Movie S1).

## 7 Nonrigid cluster simulations

In this section, we present additional results on nonrigid clusters. We observe that the cluster anisotropy observed in Fig. 2 of the main paper persists in fluid clusters, but is somewhat weaker (Fig. S5). This occurs because the rotational diffusion of pairs of cells at our nonrigid parameter set is significantly faster than that of the rigid parameter set (compare Movie S1, Movie S2). As the cluster’s polarities  $\langle \mathbf{p}^i \rangle$  are influenced by the cluster orientation over a timescale  $\tau$ , as diffusion becomes faster with respect to  $\tau$ , anisotropy decreases. We also note that we would not expect our rigid-cluster results to be precisely accurate even without this effect, as the pair’s separation will fluctuate around its equilibrium value, changing  $\mathcal{M}$ .

We presented in the main paper a figure showing how the cluster velocity and chemotactic index depend on the cluster size (Fig. 4 of the main paper). However, in Fig. 4, we treat all of the cells that were initially in contact as a single cluster, even if they broke apart – thus we are plotting velocity and CI versus the total number of cells in the simulation. An alternate way to compute a curve showing velocity and CI as a function of cluster size would be to look at a simulation in which an initially large cluster breaks into smaller clusters (as seen in [1]), and then track the smaller clusters. Doing this can yield different results, because the history of the smaller clusters matters. In particular, clusters are more likely to break off from the side of the big cluster at higher  $S$  (see e.g. Movie S2) – leading to important biases. For instance, we note in Fig. S6a that smaller clusters (which have been ejected) have a larger velocity than large ones, even though isolated small clusters are slower than isolated large clusters. Similarly, we see in Fig. S6b that even isolated cells develop an apparent chemotactic index. This occurs even though single isolated cells in our model have a behavior that is completely independent of the chemotactic signal – if a single cell is isolated for a long enough time, its dynamics will again be unbiased. Interestingly, [1] also observe that transient association with a larger cluster can cause chemotaxis – this may be a related effect.

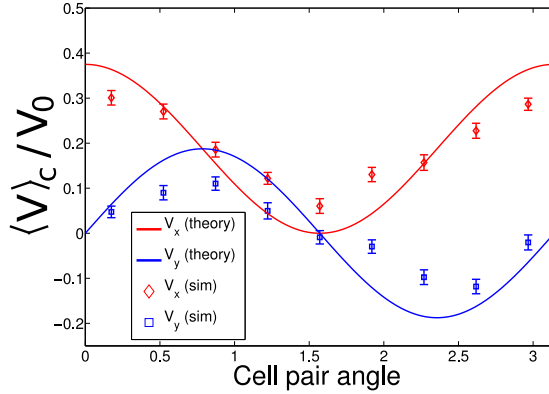


Figure S5: **Anisotropy exists but is lower in nonrigid clusters.** A pair of cells with our nonrigid cluster parameters has anisotropic chemotaxis, but with a slightly weaker anisotropy. Trajectories here are measured over the time range  $6.25\tau$  to  $50\tau$ ;  $n = 20, 200$  trajectories are simulated. Rigid cluster results are computed using a cell-cell spacing of  $0.75$  to roughly match the separation seen in simulations, so the curves plotted are  $0.75 \times \frac{1}{2} \cos^2 \theta$  and  $0.75 \times \frac{1}{2} \cos \theta \sin \theta$ .

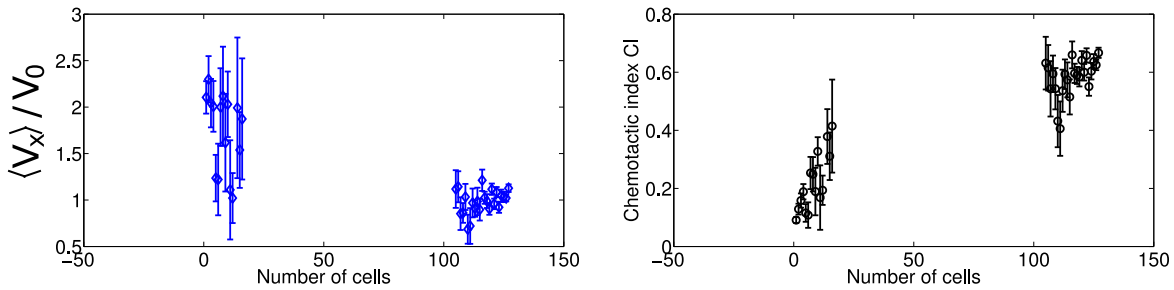


Figure S6: **Analyzing clusters in the process of breaking down can lead to apparent single-cell chemotaxis.** Tracking clusters as they break off from a larger cluster leads to an increased velocity for smaller clusters, and a non-zero chemotactic index even for single cells. This figure is generated by simulating clusters initially of  $127$  cells ( $6$ -layer oligomers) over a time of  $50\tau$  ( $1000$  minutes), and then computing the average velocity and average instantaneous chemotactic index  $V_x/|V|$  as a function of the number of cells in a given sub-cluster;  $200$  different trajectories are used. We discard the first  $25\tau$  of the trajectory, so we are focusing on the late cluster breakup stage. Two cells are considered to be in the same cluster if they are within a distance  $D_0$  of one another (e.g. the force between them is nonzero). We only show points in this figure where we have at least  $25\tau$  of trajectory time with clusters of that size totaled over all  $200$  simulations. Clusters of, e.g.  $50$  cells are not typically seen, and therefore not shown in this figure.

## 8 Numerical details of full model simulation

For our simulations, we solve the model equations numerically using a standard Euler-Maruyama scheme. For our rigid cluster simulations, we adapt the cell-cell force from [4]

$$\mathbf{F}^{ij} = \hat{\mathbf{r}}^{ij} \begin{cases} v_r (d^{ij} - 1), & d^{ij} < 1 \\ v_a \frac{d^{ij} - 1}{D_0 - 1}, & 1 \leq d^{ij} < D_0 \\ 0 & d^{ij} > D_0 \end{cases} \quad (\text{S18})$$

where  $d^{ij} = |\mathbf{r}^i - \mathbf{r}^j|$ . This force is a repulsive spring below the equilibrium separation (which is one in our units,  $20$  microns in physical units), an attractive spring above it, and vanishes above  $D_0$ .  $D_0 = 1.2$  in all of our simulations, and we use  $v_r = v_a = 500$ . This keeps the clusters very rigid.

For our non-rigid cluster simulations, we adapt the many-body force chosen by Warren to simulate vapor-liquid coexistence [5],

$$\mathbf{F}^{ij} = [Aw(d^{ij}/D_0) + B(\bar{\rho}^i + \bar{\rho}^j)w(d^{ij})] \hat{\mathbf{r}}^{ij} \quad (\text{S19})$$

where  $w(r) = (1 - r)$  for  $r \leq 1$  and  $0$  otherwise. The densities are defined by  $\bar{\rho}^i = \sum_j w_\rho(d^{ij})$ , where the sum is over all cells, including  $i$ , and  $w_\rho(r) = \frac{6}{\pi}(1 - r)^2$  for  $r \leq 1$  and  $0$  otherwise. The force of Eq. S19 is composed of an attractive force that goes to zero at a separation of  $D_0$ , and a repulsive force that is zero beyond the distance of cell-cell overlap ( $1$  in our units). Both attractive and repulsive forces have a finite value even with cells completely overlapping (“soft cores”). The strength of the repulsive force increases with increasing cell density – this makes the force explicitly dependent on many-body

interactions. This force makes developing fluid droplets relatively easy, even with short-range interactions [5], and we have found that it is more robust than Eq. S18 in creating chemotaxing non-rigid clusters. This may be because the balance of forces for edge cells is different, due to the density-dependent interactions – allowing edge cells to exert significant forces without separating from the bulk. We use  $A = -23.1$  and  $B = 7.35$  for our non-rigid cluster simulations unless otherwise noted. We chose these parameters to permit cell-cell rearrangements while still preserving cluster cohesion; the existence of collective chemotaxis does not depend on the precise values.

We initialize our clusters centered at the origin. For rigid clusters, we start our simulations with the shapes given in Table S1 but rotated to a random angle, and a spacing of the equilibrium spacing (unity) for rigid clusters. For non-rigid clusters, we start with the appropriate  $Q$ -layer cluster at a random angle, but with a spacing of 0.7. For non-rigid clusters, we initialize 2-, 3-, and 4-cell clusters by removing the appropriate number of cells randomly from the outer layer of a heptamer. In both cases, we initialize the polarity  $\mathbf{p}$  to a random value from its distribution (i.e.  $\beta^i \tau \mathbf{q}^i$  plus an appropriate noise).

## 9 Table of parameters

Parameter symbol	Name	Value in our units
$\tau$	Persistence time	1
$\sigma$	Characteristic cell speed (OU noise parameter)	1
$\bar{\beta}$	CIL strength	20 for rigid clusters, 1 for nonrigid clusters
$v_a$	Adhesion strength	500 (rigid clusters only)
$v_r$	Cell repulsion strength	500 (rigid clusters only)
$D_0$	Maximum interaction length	1.2
$S_0$	Signal strength at origin	1
$\Delta t$	Time step	$10^{-4}$ for rigid clusters, $5 \times 10^{-3}$ for nonrigid clusters
$A$	Attraction strength for Warren force (Eq. S19)	-23.1 (nonrigid clusters only)
$B$	Repulsion strength for Warren force (Eq. S19)	7.35 (nonrigid clusters only)

Table S2: **Parameters used**

## References

- [1] Eric Theveneau, Lorena Marchant, Sei Kuriyama, Mazhar Gull, Barbara Moepps, Maddy Parsons, and Roberto Mayor. Collective chemotaxis requires contact-dependent cell polarity. *Developmental Cell*, 19(1):39, 2010.
- [2] Gema Malet-Engra, Weimiao Yu, Amanda Oldani, Javier Rey-Barroso, Nir S Gov, Giorgio Scita, and Loïc Dupré. Collective cell motility promotes chemotactic prowess and resistance to chemorepulsion. *Current Biology*, 25:242, 2015.
- [3] Sangtae Kim and Seppo J Karrila. *Microhydrodynamics: principles and selected applications*. Courier Dover Publications, 2013.
- [4] Balint Szabo, GJ Szöllösi, B Gönci, Zs Jurányi, David Selmeczi, and Tamás Vicsek. Phase transition in the collective migration of tissue cells: experiment and model. *Physical Review E*, 74(6):061908, 2006.
- [5] PB Warren. Vapor-liquid coexistence in many-body dissipative particle dynamics. *Physical Review E*, 68(6):066702, 2003.